

1

2

*Geophysical Research Letters*

3

Supporting Information for

4

**Advancing Atmospheric River Forecasts into Subseasonal-to-Seasonal Timescales**

5

Cory F. Baggett<sup>1</sup>, Elizabeth A. Barnes<sup>1</sup>, Eric D. Maloney<sup>1</sup>, and Bryan D. Mundhenk<sup>1</sup>

6

<sup>1</sup>Department of Atmospheric Science, Colorado State University, Fort Collins, CO, USA

7

8

**Contents of this file**

9

- 10      Text S1. Atmospheric river characteristics
- 11      Text S2. MJO index
- 12      Text S3. QBO index
- 13      Text S4. Calculation of IVT
- 14      Text S5. Atmospheric river detection algorithm
- 15      Text S6. Definition of IVT<sub>AR</sub>
- 16      Text S7. ECMWF reforecast ensemble system data
- 17      Text S8. Logarithmic skill score calculation
- 18      Text S9. Testing for Independence from ENSO
- 19      Text S10. Data repositories
- 20      Text S11. Statistical significance via Monte Carlo Simulations
- 21
- 22
- 23      Figures S1 to S7
- 24      Tables S1 to S6

25     **Introduction**

26         Throughout the supporting text, we provide a more detailed overview of the defining  
27         characteristics of ARs (Text S1), definitions of the MJO and QBO indices used throughout this  
28         study (Texts S2 and S3), the formula used for the calculation of IVT (Text S4), details on the AR  
29         detection algorithm (Text S5), a definition of  $\text{IVT}_{\text{AR}}$  (Text S6), an overview of the ECMWF  
30         reforecast ensemble system data (Text S7), the formulas used to calculate the LSS and an  
31         example of their application (Text S8), a test to show our results are independent from ENSO's  
32         influence (Text S9), the location of the data repositories used in this study (Text S10), and a brief  
33         explanation of the Monte Carlo simulation we employ to test for statistical significance (Text  
34         S11).

35         In the supporting figures, we display results for AR activity for California and an expanded  
36         Pacific Northwest that includes Northern California (Figures S1-S4); a composite of anomalous  
37         AR strikes per week based only on the MJO (Figure S4); a composite of anomalous AR strikes  
38         per week based on the MJO using the RMM index and the QBO (Figure S5); easterly minus  
39         westerly QBO composites of anomalous 500-hPa geopotential heights and  $\text{IVT}_{\text{AR}}$  shown weekly  
40         as a function of MJO phase (Figures S6); and compare easterly minus westerly QBO composites  
41         of anomalous 500-hPa geopotential heights,  $\text{IVT}_{\text{AR}}$ , and OLR to La Niña minus El Niño  
42         composites of these same variables (Figures S7).

43         The supporting Tables provide sample sizes (Tables S1-S3, S5, and S6) and the values  
44         corresponding to an example calculation of the LSS (Table S4).

45

46     **Text S1. Atmospheric river characteristics**

47         ARs [*Gimeno et al.*, 2014; *Ralph and Dettinger*, 2011] are typically defined as being long ( $>$   
48         2000 km) and narrow ( $< 1000$  km) regions of intense atmospheric moisture transport. They  
49         usually have total column water values exceeding  $20 \text{ kg m}^{-2}$  and are characterized by extreme  
50         values of vertically integrated vapor transport (IVT). ARs can transport moisture over long

51 distances and account for ~90% of the poleward moisture transport in the mid-latitudes. An AR's  
52 moisture may derive from the tropics and sub-tropics, but they may also collect moisture through  
53 in situ horizontal convergence and surface evaporation. Oftentimes, ARs are associated with the  
54 warm conveyors belts of synoptic-scale cyclones [Baggett *et al.*, 2016; Sodemann and Stohl,  
55 2013].

56

## 57 **Text S2. MJO index**

58 Indices that define the MJO consist typically of 8 phases that roughly correspond to the  
59 geographic location where active tropical convection resides. Two such indices are the Real-time  
60 Multivariate MJO Index (RMM) [Wheeler and Hendon, 2004] and the outgoing longwave  
61 radiation (OLR)-based MJO Index (OMI) [Kiladis *et al.*, 2014]. Throughout this study, we use  
62 the OMI, which we acquire from the Earth System Research Laboratory/Physical Sciences  
63 Division/NOAA. It is calculated by projecting the 20-96 day band-passed filtered OLR onto the  
64 two leading empirical orthogonal functions of the 30-96 day eastward band-passed filtered OLR.  
65 This yields two principal component time series (PC1 and PC2) from which the phase and  
66 amplitude of the OMI may be derived. We test the sensitivity of our results to the choice of MJO  
67 index, and find our results remain qualitatively the same (compare Figures 3 and S5). To make  
68 the phase space of the OMI geographically consistent with the phase space of the more  
69 traditionally used RMM, we multiply PC1 by -1 and reverse the ordering of PC1 and PC2. In this  
70 study, we only consider days when the MJO amplitude is  $\geq 1$  (i.e.,  $\sqrt{PC1^2 + PC2^2} \geq 1$ ).

71

## 72 **Text S3. QBO index**

73 We calculate a monthly QBO index [Yoo and Son, 2016] to classify days that occur during  
74 easterly or westerly phases of the QBO. We area-average between 10°S and 10°N monthly-mean  
75 values of  $u$  at 50-hPa. Then, monthly anomalies are calculated by subtracting from a given month

76 its monthly climatological value (averaged across 1979–2015). A three-month running average is  
77 then taken of these monthly anomalies. Months when the standard deviation of this anomaly is  
78 greater than 0.5 (less than -0.5) are considered westerly (easterly) QBO periods.

79

80 **Text S4. Calculation of IVT**

81 IVT is calculated according to

82 
$$IVT = \sqrt{\left(\frac{1}{g} \int_{1000hPa}^{300hPa} u q dp\right)^2 + \left(\frac{1}{g} \int_{100hPa}^{300hPa} v q dp\right)^2},$$

83 where  $u$  and  $v$  are the zonal and meridional winds, respectively,  $q$  is the specific humidity,  $g$  is the  
84 acceleration of gravity, and  $dp$  is the difference between pressure levels. Anomalous values of  
85 IVT and other variables are found by subtracting their calendar day mean. The calendar day mean  
86 has been smoothed by applying a fast Fourier transform to its raw annual cycle and retaining only  
87 the first two harmonics.

88

89 **Text S5. Atmospheric river detection algorithm**

90 Two differing approaches have been used by recent studies to detect atmospheric rivers: one  
91 based on some measure of integrated water vapor content [*Dettinger et al.*, 2011; *Ralph et al.*,  
92 2004; *Wick et al.*, 2013] and one based on IVT [*Guan and Waliser*, 2015; *Payne and*  
93 *Magnusdottir*, 2014; *Zhu and Newell*, 1998]. The ARs evaluated in this work are objectively  
94 identified using a detection algorithm [*Mundhenk et al.*, 2016a; *Mundhenk et al.*, 2016b]  
95 that fits into the latter category. The original algorithm is available for download at  
96 <http://hdl.handle.net/10217/170619>.

97 The algorithm uses fields of positive anomalous IVT, together with a series of intensity and  
98 geometric tests (e.g., mean intensity, total area, length, length-to-width ratio), to detect and retain  
99 only those features that are plume-like in nature and of the appropriate spatial scale. Here, the use  
100 of anomalies benefits automated feature detection within large spatial and temporal domains, and

101 also affords the use a of static IVT anomaly threshold. Throughout this work, a static anomalous  
102 IVT magnitude threshold of  $\sim 183 \text{ kg m}^{-1} \text{ s}^{-1}$  is used to isolate features of interest. This value  
103 represents the 94th percentile of the all-season distribution of daily IVT anomaly values over the  
104 North Pacific Ocean calculated from ERA-Interim. This anomaly threshold is used for AR  
105 detection within both the ERA-Interim reanalysis dataset and the ECMWF reforecasts. We  
106 calculate an IVT threshold derived directly from the ECMWF reforecasts and find it to have a  
107 very similar value to that of ERA-Interim and ultimately little impact on AR detection.

108 Compared to a prior version of the AR detection algorithm [Mundhenk *et al.*, 2016a], the  
109 version employed in this work does not contain the multiple peak logic that scrutinizes  
110 “connected” features within fields of anomalous IVT. The mid- and high-latitude results analyzed  
111 in this work are generally insensitive to the removal of this logic test.

112 The AR detection algorithm employs an occurrence-based approach (i.e., one AR is  
113 recorded for each period during which the criteria are satisfied), wherein each time step is  
114 scrutinized independently. As a result, the numbers of AR strikes described within this work are  
115 calculated based on the number of days during which AR-like conditions exists over a given  
116 boundary.

117

#### 118 **Text S6. Definition of $\text{IVT}_{\text{AR}}$**

119  $\text{IVT}_{\text{AR}}$  is the IVT associated with ARs. To create a daily map of  $\text{IVT}_{\text{AR}}$ , we multiply a daily  
120 IVT map by its daily mask. The daily mask has a value of 1 everywhere an AR exists (according  
121 to the AR detection algorithm) and a value of 0 elsewhere. Calendar day means of  $\text{IVT}_{\text{AR}}$  are  
122 calculated from such maps, from which daily anomalies of  $\text{IVT}_{\text{AR}}$  are derived. Thus, a given daily  
123 map of anomalous  $\text{IVT}_{\text{AR}}$  has positive values everywhere an AR exists on that day and negative  
124 values or zero everywhere an AR is absent.

125

126 **Text S7. ECMWF reforecast ensemble system data**

127 We acquire ECMWF reforecasts from ECMWF's S2S data library [Vitart *et al.*, 2017], a  
128 deliverable of the S2S Project established by the World Weather Research Program/World  
129 Climate Research Program (WWRP/WCRP). The ECMWF reforecast ensemble system consists  
130 of 11 members – one control run and 10 perturbed runs. Complete details of ECWMF reforecast  
131 ensemble system [Vitart *et al.*, 2017] and the S2S Project in general may be found online at  
132 <https://software.ecmwf.int/wiki/display/S2S/Models>. From the data library we obtain daily  
133 (instantaneous 0000 UTC) values of  $u$ ,  $v$ , and  $q$  at a horizontal resolution of  $1.5^\circ$  by  $1.5^\circ$  and a  
134 vertical resolution of six pressure levels located at 1000, 925, 850, 700, 500, and 300 hPa. Each  
135 reforecast spans 46 days. On a given calendar date, reforecasts are made for the prior 20 years.  
136 The ECMWF reforecast models are considered “on-the-fly,” meaning that ECMWF continually  
137 updates its model each time reforecasts are made. In this study, we use reforecasts that have  
138 initialization dates that fall during November through February, spanning from 2 November 1995  
139 to 28 February 2015. In total, we use 1346 reforecasts, at a frequency of ~4 initializations per  
140 week.

141

142 **Text S8. Logarithmic skill score calculation**

143 The logarithmic score (LS) [Roulston and Smith, 2002; Tippett *et al.*, 2017] is a local,  
144 strictly proper scoring method. Because it is a local score, the LS depends only on the probability  
145 of the forecast category that is observed. Because it is strictly proper, the LS cannot be  
146 manipulated or hedged – the forecast system must predict its true belief [Roulston and Smith,  
147 2002; Tippett *et al.*, 2017; Wilks, 2011]. Furthermore, the LS rewards the forecaster for having  
148 additional forecast categories. This is particularly useful in forecasting AR strikes per week, as  
149 there are naturally 8 different outcomes (integers ranging from 0 to 7 because our data has a daily  
150 temporal resolution) that can be assigned probabilities by the forecast system.

151 To calculate the logarithmic skill score (LSS) in an ensemble framework, a forecast  
152 probability  $p_i$  is assigned to each forecast category  $c_i$  of possible AR strikes on a given region  
153 during a given week. For example,  $p_0$  corresponds to the forecasted probability that  $c_0 = 0$  AR  
154 strikes occur during a given week, whereas  $p_7$  corresponds to the forecasted probability that  $c_7 = 7$   
155 AR strikes occur (i.e., an AR strike on each day during a given week). We define  $p_i$  according to

156 
$$p_i = \frac{n_i + C^{-1}}{N + 1}$$

157 where  $n_i$  is the number of ensemble members that forecast  $c_i$ ,  $C$  is the total number of categories  
158 (here, 8), and  $N$  is the total number of ensembles (here, 11, corresponding to the 1 control run and  
159 the 10 perturbed runs from the ECMWF reforecast ensemble system) [Tippett *et al.*, 2017]. This  
160 formulation of  $p_i$  ensures that forecast probabilities of 0 and 1 do not occur. To compute the LS of  
161 the forecast,

162 
$$\text{LS} = \log p_i$$

163 where  $i$  corresponds to the category in which the actual observation falls. The LSS is determined  
164 by

165 
$$\text{LSS} = \overline{\text{LS}} - \overline{\text{LS}}_{\text{ref}}$$

166 where the overbar denotes averaging over multiple reforecasts.  $\text{LS}_{\text{ref}}$  refers to the LS of a  
167 reference forecast based on the climatological AR strike probabilities  $q_i$ . To find  $q_i$  for a given  
168 calendar day, we count the number of times  $i$  strikes per week is observed during the 91-day  
169 window centered on that calendar day, spanning the years 1979-2015, and divide by the total  
170 number of days examined. Thus,  $q_i$  is simply a function of calendar day and is independent of the  
171 phases of the MJO and the QBO.

172 Table S4 provides an example of calculating the LSS for a single reforecast model run that  
173 initialized at 0000 UTC 3 December 2009. We calculate the LSS for AR strikes on Alaska during  
174 the first week of the model run (4 to 10 December 2009). The actual observed number of strikes  
175 during this week was 3 (highlighted row in Table S1). Five of the 11 members of the ECMWF

176 reforecast ensemble system predicted 3 AR strikes to occur during that week, yielding  $p_3 \approx 0.43$ .  
177 The climatological probability of 3 AR strikes occurring is  $q_3 \approx 0.11$ . Thus,  $LS \approx -0.85$ ;  $LS_{ref} \approx -$   
178 2.19; and  $LSS \approx 1.34$ . In this case, the ECMWF reforecast ensemble system is clearly more  
179 skillful than a climatological forecast.

180 In Figures 4 and S3,  $C$  varies as a function of lead time. At lead times  $d \geq 7$ ,  $C = 8$  forecast  
181 categories are used to calculate the LSS. For lead times  $d < 7$ ,  $C = d + 1$  forecast categories are  
182 used to calculate the LSS. For example,  $d = 3$  has  $C = 4$  forecast categories corresponding to the  
183 probabilities that 0, 1, 2, or 3 AR strikes occur during the 3 day period prior to and inclusive of  $d$   
184 = 3.

185

#### 186 **Text S9. Testing for independence from ENSO**

187 The El Niño-Southern Oscillation (ENSO) is the dominant mode of interannual variability  
188 in the tropics. Therefore, it is reasonable to ask if the modulation of AR activity by the MJO and  
189 the QBO on display in our results is being heavily influenced by ENSO. This question was also  
190 asked by *Yoo and Son* (2016) and *Son et al.* (2017). They found that the QBO modulates the MJO  
191 independent of ENSO. Nevertheless, it is a worthwhile endeavor to test for ENSO independence  
192 in the context of our own results. To this end, we use the Niño3.4 index acquired from the  
193 National Centers for Environmental Prediction/Climate Prediction Center. The Niño3.4 index is a  
194 monthly time series of anomalous sea surface temperatures (SSTs) in an area-averaged box  
195 located in the central, tropical Pacific Ocean (170°W to 120°W and 5°S to 5°N). Niño3.4 months  
196 are designated as either El Niño or La Niña when the three-month running mean of five  
197 sequential and overlapping three-month periods have SST anomalies that are greater than 0.5°C  
198 or less than -0.5°C, respectively. Neutral conditions are said to exist if neither El Niño nor La  
199 Niña are active.

200 Our first test is to classify each November through February month from 1979-2015 by its  
201 combined QBO and ENSO state. Once classified, we count the months and display the results in

202 Table S5. During easterly QBO periods, ENSO conditions were neutral during 25 months, while  
203 El Niño and La Niña conditions occurred during 9 and 12 months, respectively. During westerly  
204 QBO periods, ENSO conditions were neutral during 27 months, while El Niño and La Niña  
205 conditions occurred during 26 and 18 months, respectively. These results suggest the possibility  
206 that a small La Niña signal may be imbedded in our easterly QBO composites and a small El  
207 Niño signal within our westerly QBO composites.

208 To investigate the extent to which there is an imbedded ENSO signal within our composites,  
209 we create Figure S7 which displays the differences between the easterly QBO composites and the  
210 westerly QBO composites (left and right-middle columns) and the differences between the La  
211 Niña composites and the El Niño composites (left-middle and right columns). Several features are  
212 noteworthy. First, with respect to the ENSO composites, there is a clear and consistent  
213 modulation of the Aleutian Low across all phases of the MJO (left-middle column). During El  
214 Niño, the Aleutian Low is deepened and vice versa during La Niña. Secondly, as a result of the  
215 deepened Aleutian Low during El Niño, there is anomalously high AR activity centered along the  
216 U.S West Coast. Comparing the ENSO composites to the QBO composites (left column), we find  
217 a much weaker amplification of the Aleutian Low and a much greater variability in its strength  
218 across all MJO phases for a given QBO phase. The variability in the Aleutian Low leads directly  
219 to a greater variability in AR strike locations along the entire west coast of North America. This  
220 contrasts starkly to the ENSO composites and suggests that ENSO is not heavily influencing the  
221 background flow in the QBO composites.

222 We make one final test for ENSO independence by compositing anomalous outgoing  
223 longwave radiation (OLR; acquired from ERA-Interim) according to the QBO (right-middle  
224 column) and ENSO (right column). Negative (positive) values of anomalous OLR indicate  
225 enhanced (reduced) convection. For the ENSO composites, there is a clear and consistent  
226 modulation of convection along the equator across all phases of the MJO. As expected with El  
227 Niño, there is enhanced convection in the Niño3.4 region. Conversely, La Niña has reduced

228 convection in the Niño3.4 region, while convection is enhanced in the Western Pacific. These  
229 convective signals dominate to the extent that they obscure the convective signals typically  
230 associated with certain phases of the MJO [Wheeler and Hendon, 2004; Kiladis *et al.*, 2014].  
231 However, these signals are practically absent when we composite against the QBO (right-middle  
232 column).

233 From these tests, we conclude that ENSO has only a minor influence on our results.  
234 However, we wish to emphasize that the modulation of AR strike activity that we observe when  
235 the MJO is segregated by QBO phase does not necessarily mean that the QBO is the direct cause  
236 of the modulation. Further research and modeling studies will shed light on the physical  
237 mechanisms that may or may not exist behind this modulation. For now, we simply observe that  
238 the modulation exists and is consequential when forecasting ARs at extended lead times.

239

#### 240 **Text S10. Data repositories**

241 ERA-Interim data [Dee *et al.*, 2011] is acquired (accessed 8 September 2016) from the  
242 European Centre for Medium-Range Weather Forecasts public datasets, available online at  
243 <http://apps.ecmwf.int/datasets/data/interim-full-daily/levtype5sf/>

244 The ECMWF reforecast ensemble system data [Vitart *et al.*, 2017] is acquired (accessed 19  
245 August 2016) from the European Centre for Medium-Range Weather Forecasts S2S prediction  
246 project public dataset, available online at [http://apps.ecmwf.int/datasets/data/s2s-reforecasts-](http://apps.ecmwf.int/datasets/data/s2s-reforecasts-instantaneous-accum-ecmf/levtype=pl/type=cf/)  
247 [instantaneous-accum-ecmf/levtype=pl/type=cf/](http://apps.ecmwf.int/datasets/data/s2s-reforecasts-instantaneous-accum-ecmf/levtype=pl/type=cf/)

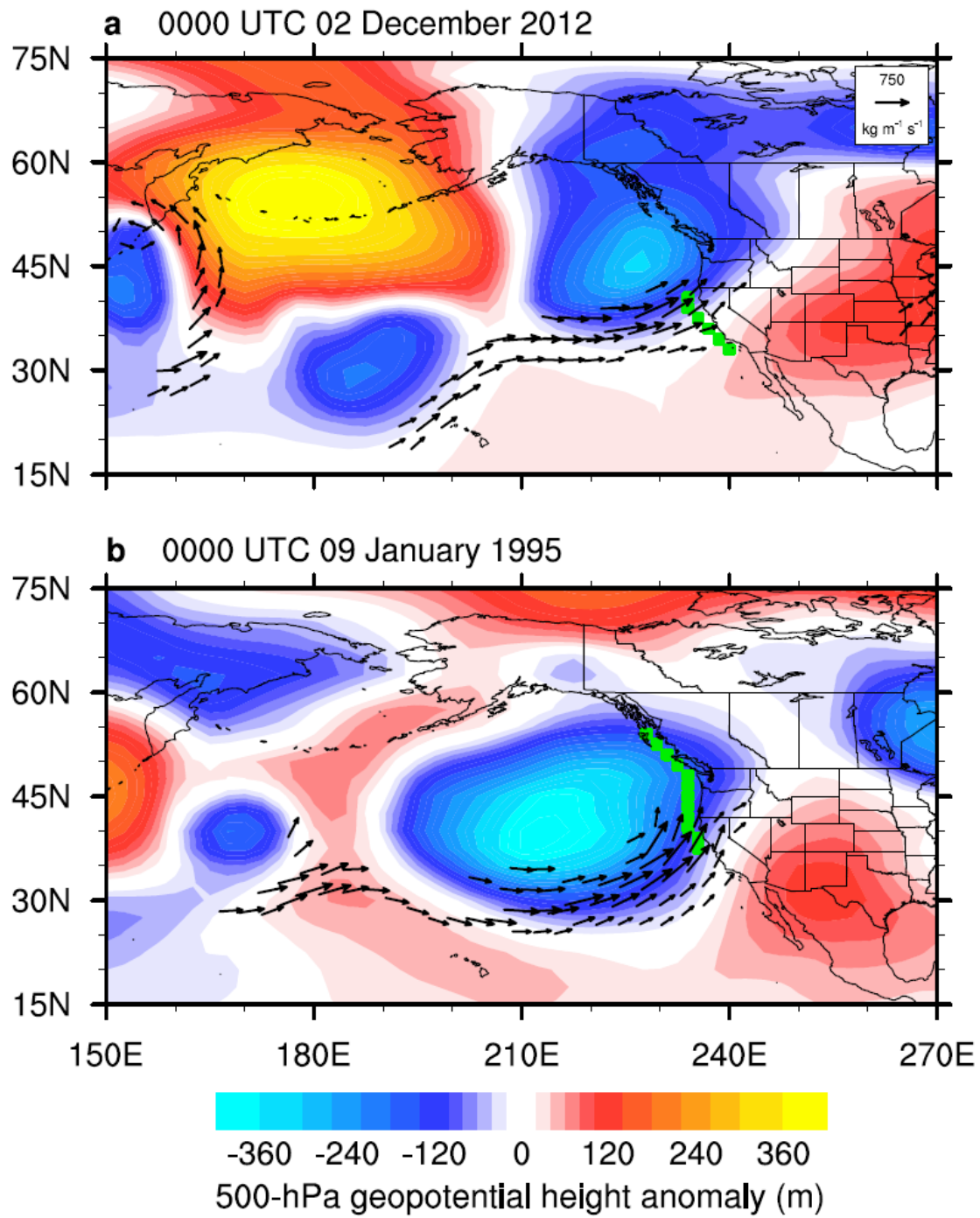
248 RMM data [Wheeler and Hendon, 2004] is acquired (accessed 11 October 2016) from the  
249 Australian Government Bureau of Meteorology Madden-Julian Oscillation monitoring site,  
250 available online at <http://www.bom.gov.au/climate/mjo/>

251 OMI data [Kiladis *et al.*, 2014] is acquired (accessed 6 January 2017) from the Earth System  
252 Research Laboratory / Physical Sciences Division of NOAA, available online at  
253 <https://www.esrl.noaa.gov/psd/mjo/mjoindex/>

254

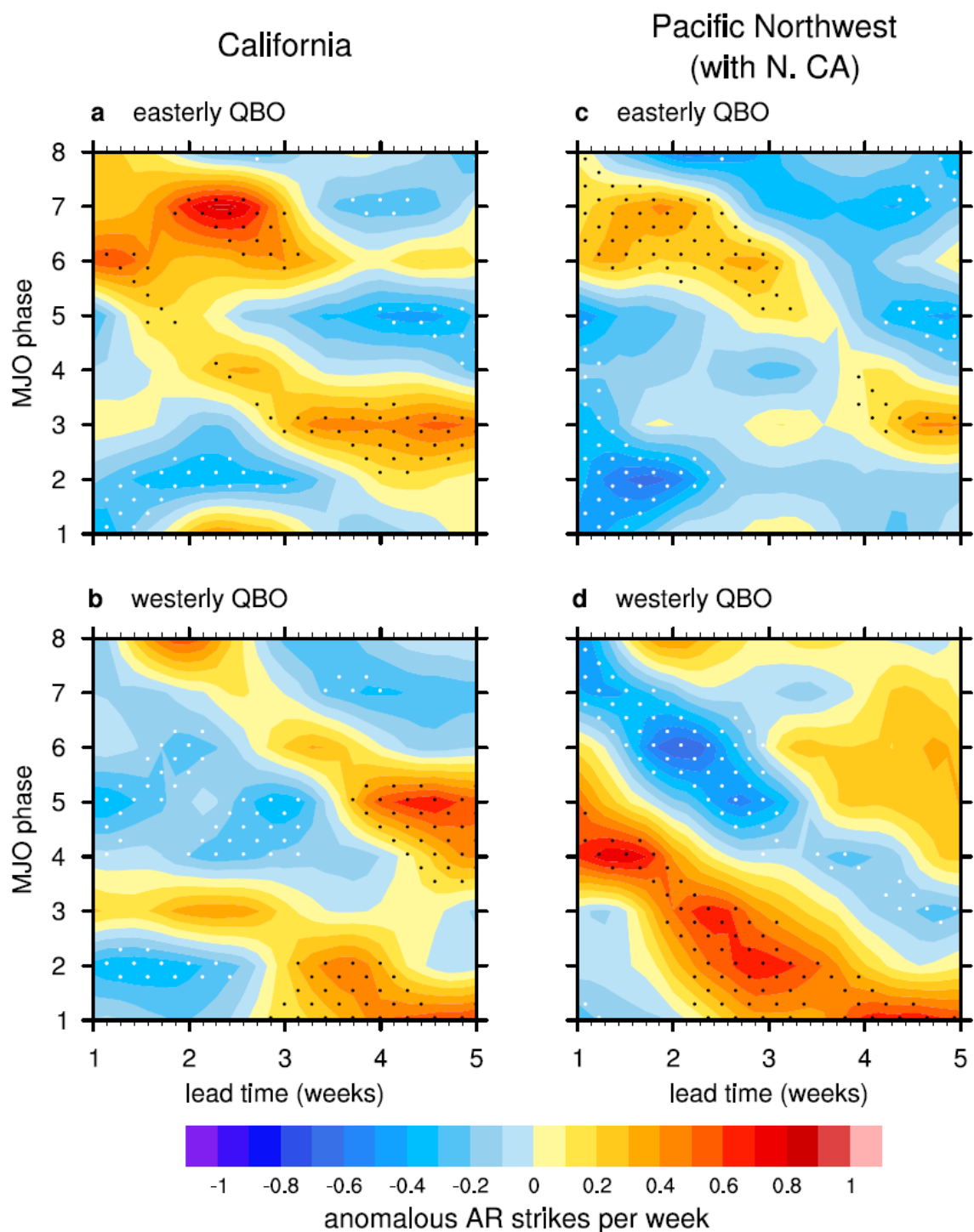
255 **Text S11. Statistical significance via Monte Carlo Simulations**

256 To test statistical significance in Figures S2, S6 and S7, we use a Monte Carlo simulation  
257 with 1000 random samples. Because the MJO may reside in a certain phase several consecutive  
258 days in a row, our composites have a certain degree of autocorrelation imbedded in them. To  
259 correct for this, we determine an equivalent sample size  $n_{eq}$  by designing our simulation to choose  
260 random samples that contain groupings of consecutive days in a row that match in number and  
261 length the groupings from the original sample.



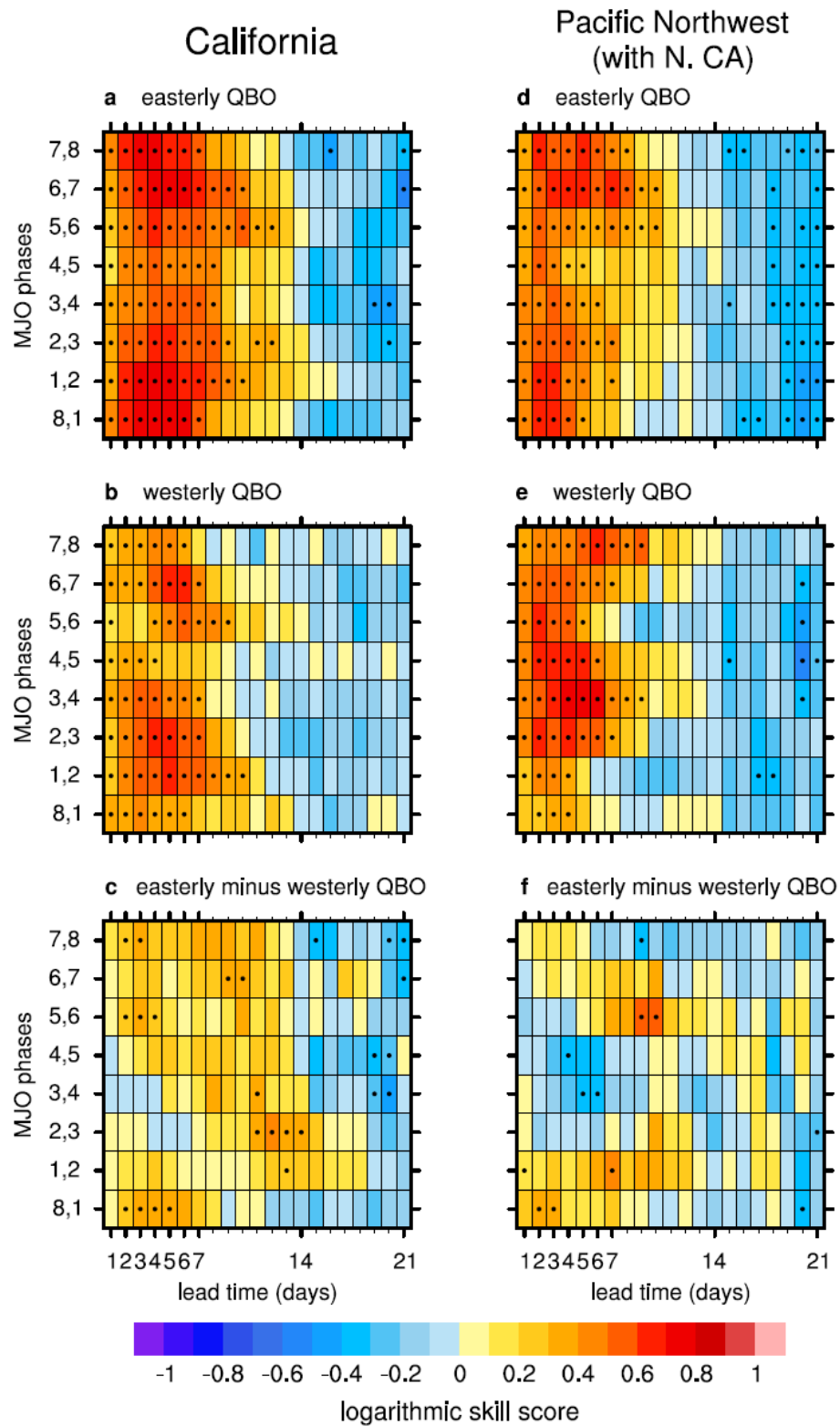
262

263 **Figure S1.** AR strike events are shown for **(a)** California at 0000 UTC 02 December 2012 during  
264 an easterly QBO period and **(b)** an expanded Pacific Northwest which includes Northern  
265 California at 0000 UTC 09 January 1995 during a westerly QBO period. Black vectors depict  
266 IVT<sub>AR</sub> ( $\text{kg m}^{-1} \text{s}^{-1}$ ). A reference vector is located in the upper right corner of **(a)**. Shading depicts  
267 500-hPa geopotential height anomalies. The grid points in green specify the particular grid points  
268 used to identify ARs that strike **(a)** California and **(b)** an expanded Pacific Northwest which  
269 includes Northern California. The figure derives from ERA-Interim data [Dee *et al.*, 2011].

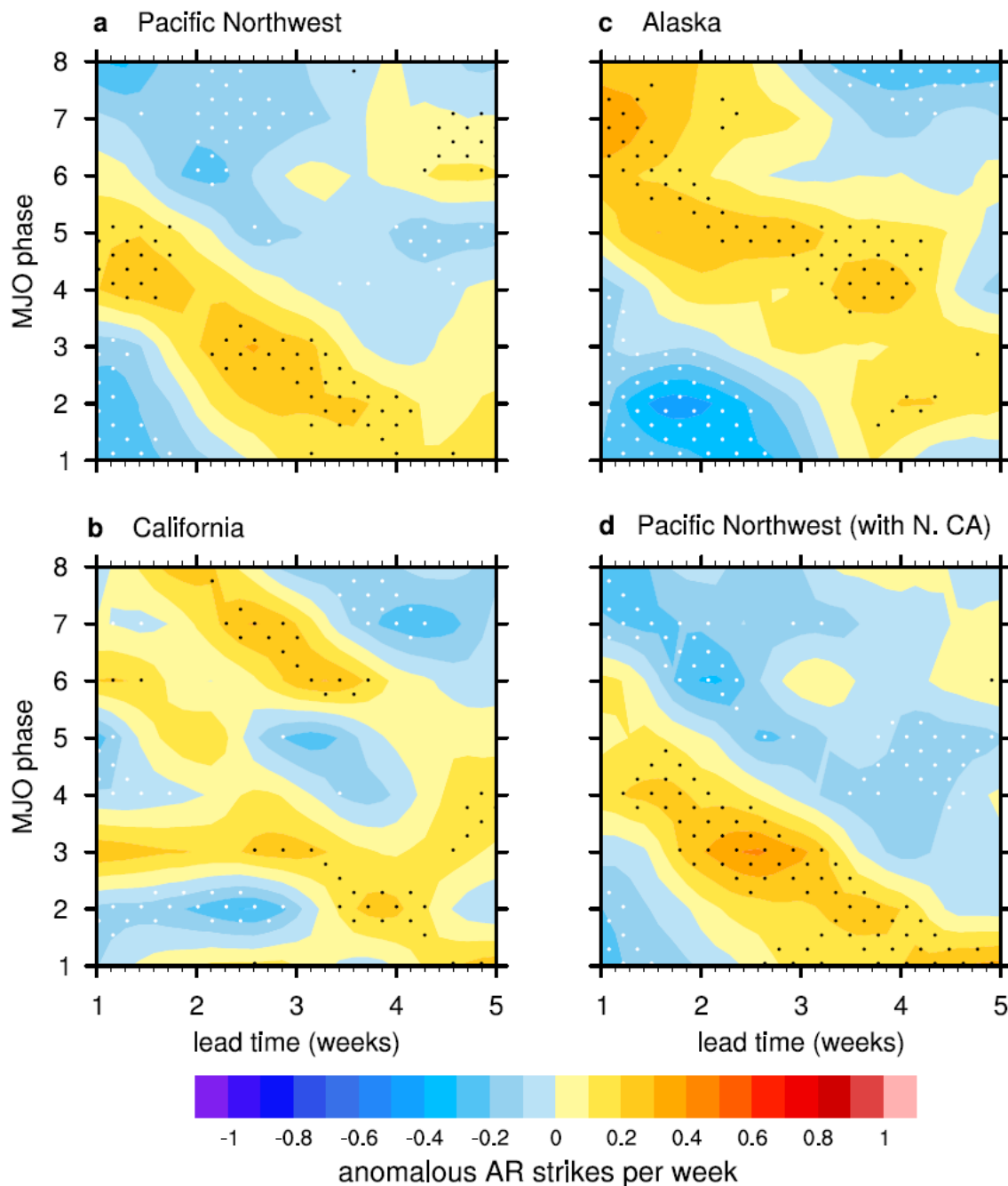


270

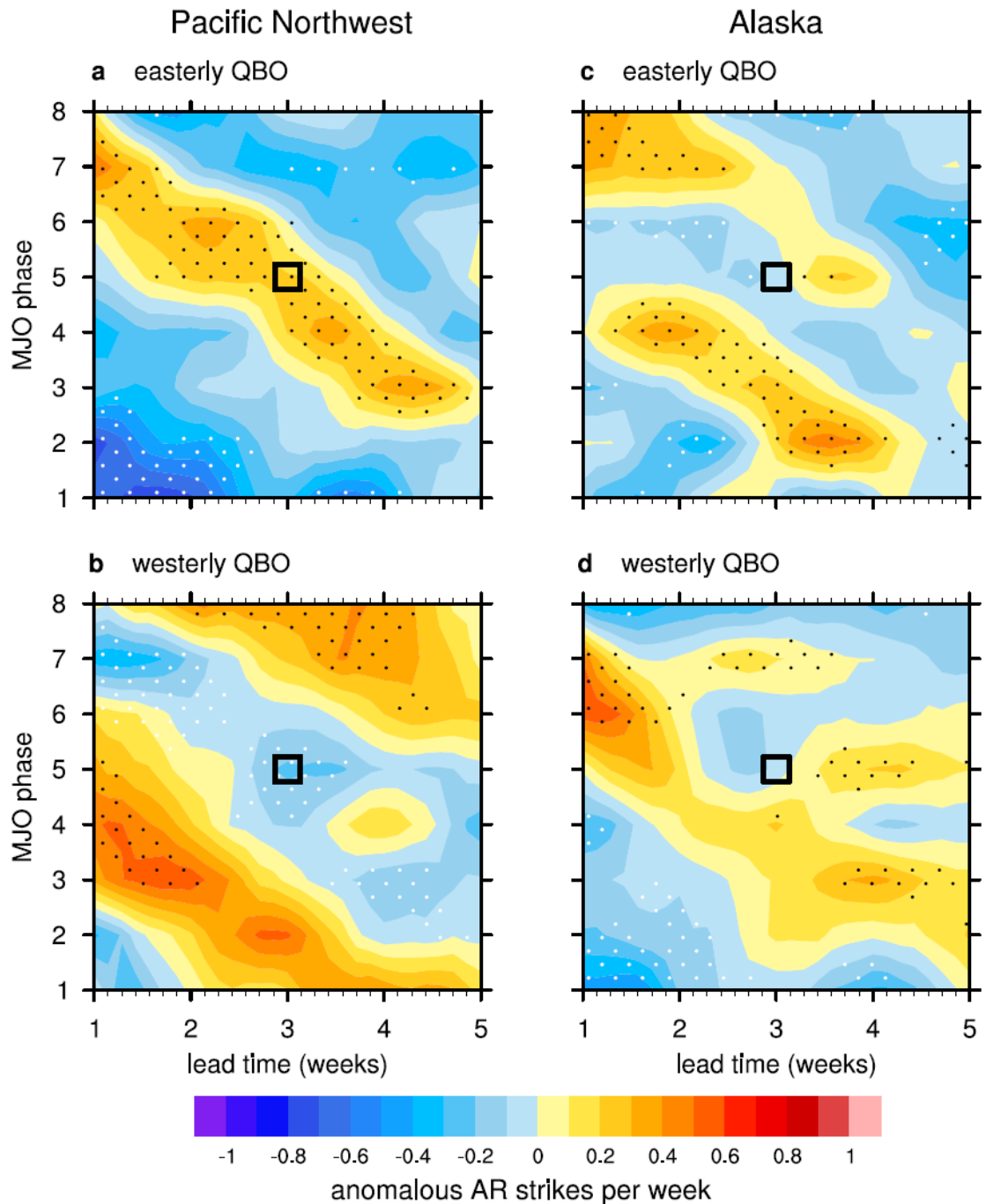
271   **Figure S2.** Observational composites are shown of anomalous AR strikes per week following  
272   days when the MJO was in a particular phase for (**a**) California and (**c**) an expanded Pacific  
273   Northwest which includes Northern California during easterly QBO periods and for (**b**) California  
274   and (**d**) an expanded Pacific Northwest which includes Northern California during westerly QBO  
275   periods. Only days during November–February are composited. The detection grid points for  
276   California and an expanded Pacific Northwest which includes Northern California are specified in  
277   Figures S1a and S1b, respectively. The ordinate indicates the MJO phase of the days being  
278   composited; the abscissa indicates the lead time (weeks) that passes between the occurrence of a  
279   particular MJO phase and the anomalous AR strikes during that week. To demonstrate  
280   robustness, each panel has its grid points ranked according to the percentage of individual  
281   anomalous AR strikes per week values that are positive within the composite. Black stippling is  
282   overlaid on the top 20% of these ranked grid points; white stippling is overlaid on the bottom  
283   20%. Sample sizes are provided in Table S1. The figure derives from [Dee *et al.*, 2011].



285   **Figure S3.** Logarithmic skill scores of the ECMWF reforecast ensemble system are shown for **(a**  
286   to **c**) California and **(d to f)** an expanded Pacific Northwest which includes Northern California,  
287   for **(a)** and **(d)** during easterly QBO periods, for **(b)** and **(e)** during westerly QBO periods, and for  
288   **(c)** and **(f)** the easterly minus the westerly QBO periods. Only the LSSs of reforecasts that  
289   initialized during November–February are calculated. The ordinate indicates the MJO phases  
290   (paired to increase sample sizes) of the initialization dates of the reforecasts; the abscissa  
291   indicates the lead time (days) that passes between the occurrence of a particular MJO phase and  
292   the final day of the forecast period (see Methods). In **(a)**, **(b)**, **(d)**, and **(e)** positive values signify  
293   the model has more skill than a climatological reference forecast. Dots indicate their difference is  
294   statistically significant at the 5% level. In **(c)** and **(f)** positive values signify that the model has  
295   more skill during the easterly QBO than the westerly QBO. Dots indicate their difference is  
296   statistically significant at the 5% level. Statistical significance is determined by a two-sided  
297   student’s t-test. Sample sizes are provided in Table S2. The figure derives from ERA-Interim data  
298   [*Dee et al.*, 2011] and ECWMF ensemble prediction system data [*Vitart et al.*, 2017].



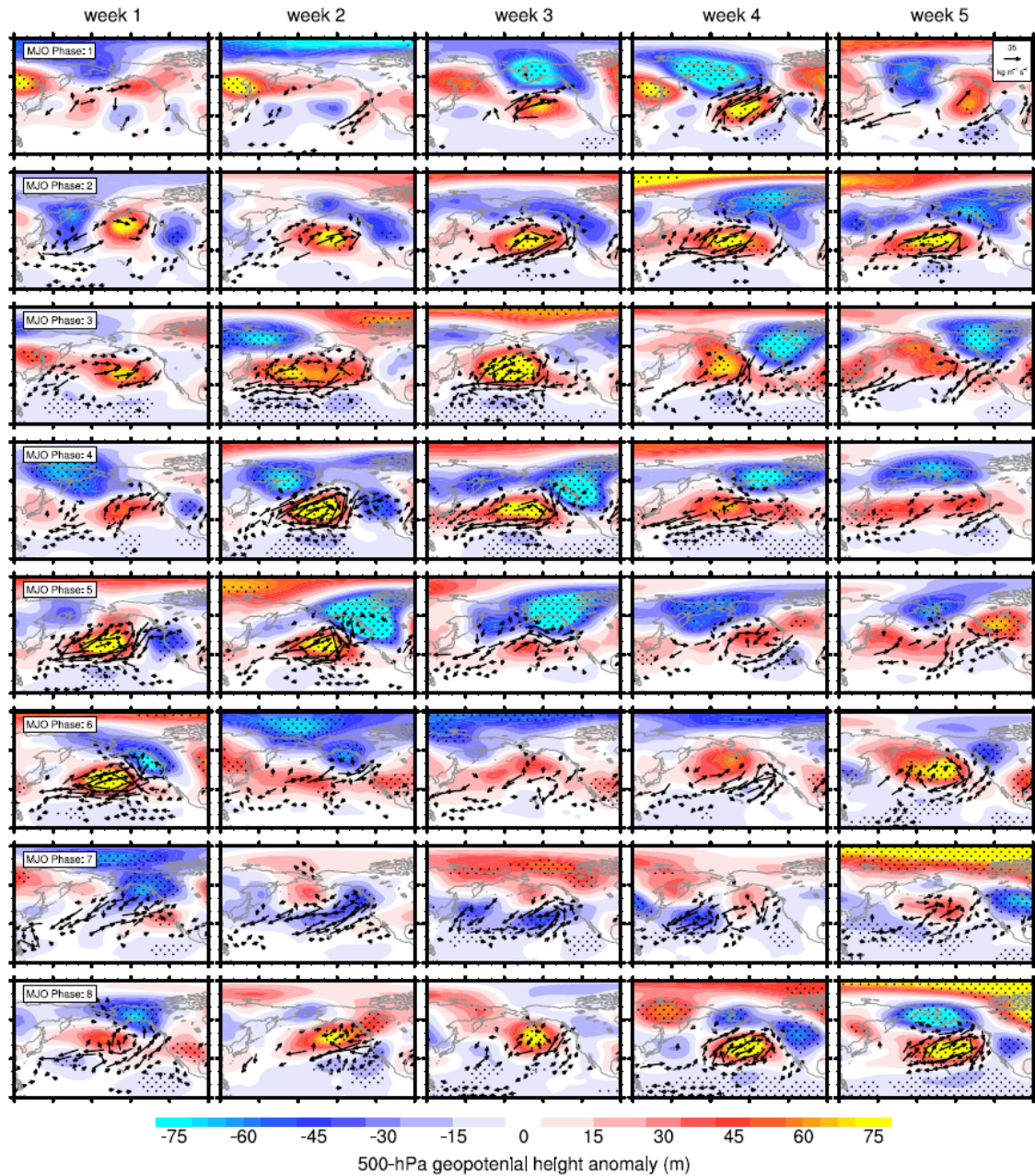
300 **Figure S4.** Observational composites are shown of anomalous AR strikes per week following  
301 days when the MJO was in a particular phase for (**a**) the Pacific Northwest, (**b**) California, (**c**)  
302 Alaska, and (**d**) an expanded Pacific Northwest which includes Northern California during all  
303 periods (independent of the phase of the QBO). Only days during November–February are  
304 composited. The detection grid points for the Pacific Northwest and Alaska are specified in  
305 Figures 1a and 1b, respectively; the detection grid points for California and an expanded Pacific  
306 Northwest which includes Northern California are specified in Figures S1a and S1b, respectively.  
307 The ordinate indicates the MJO phase of the days being composited; the abscissa indicates the  
308 lead time (weeks) that passes between the occurrence of a particular MJO phase and the  
309 anomalous AR strikes during that week. To demonstrate robustness, each panel has its grid points  
310 ranked according to the percentage of individual anomalous AR strikes per week values that are  
311 positive within the composite. Black stippling is overlaid on the top 20% of these ranked grid  
312 points; white stippling is overlaid on the bottom 20%. Sample sizes are provided in Table S1. The  
313 figure derives from ERA-Interim data [*Dee et al., 2011*].



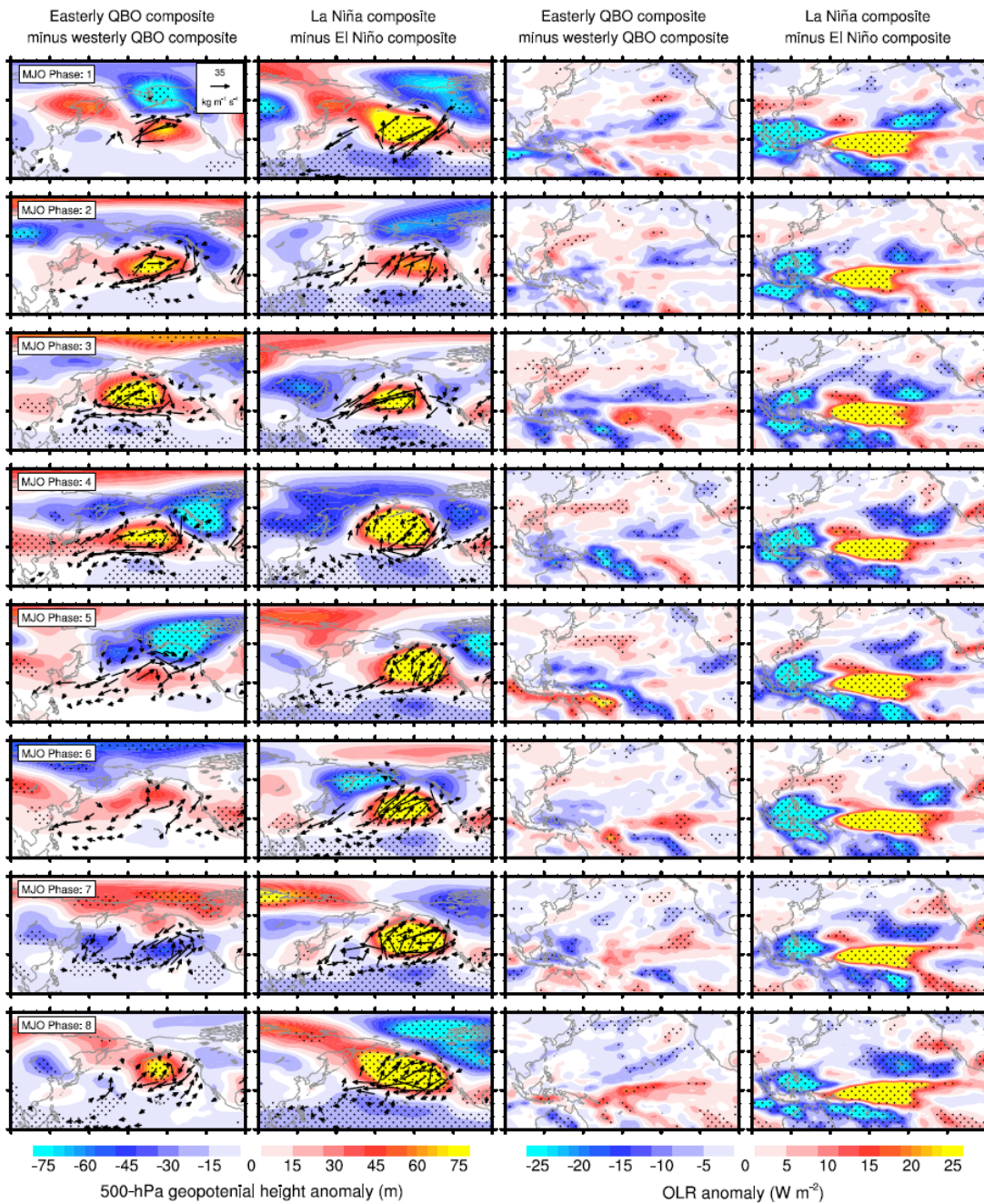
314

315 **Figure S5.** As in Fig. 3 but we use the RMM index rather than the OMI to composite by MJO  
316 phase. The RMM index [Wheeler and Hendon, 2014] is obtained from the Australian  
317 Government Bureau of Meteorology. Sample sizes are provided in Table S3.

### Easterly QBO composite minus westerly QBO composite



319 **Figure S6.** Easterly QBO composites minus westerly QBO composites are shown following each  
320 phase of the MJO. Each row corresponds to a phase of the MJO where the (**Left column**) is  
321 averaged over week 1; the (**Left-middle column**) is averaged over week 2; the (**Middle column**)  
322 is averaged over week 3; the (**Right-middle column**) is averaged over week 4; and the (**Right**  
323 **column**) is averaged over week 5. The displayed longitudinal range is from 120°E to 270°E; the  
324 display latitudinal range is from the equator to 90°N. Only days during November–February are  
325 composited. Black vectors depict anomalous IVT<sub>AR</sub> ( $\text{kg m}^{-1} \text{s}^{-1}$ ), with only those vectors with  
326 magnitudes  $\geq 10 \text{ kg m}^{-1} \text{s}^{-1}$  and with either component statistically significant at the 2% level  
327 plotted. A reference vector is located in the upper right corner of the (**top-right panel**). Two  
328 iterations of nine-point local smoothing were applied to the components of the vectors before  
329 plotting. Shading depicts 500-hPa geopotential height anomalies, with its statistical significance  
330 at the 2% level indicated by stippling, as determined by a Monte Carlo simulation (Text S11).  
331 Sample sizes are provided in Table S1. The figure derives from ERA-Interim data [*Dee et al.*,  
332 2011].



333

334 **Figure S7.** Differences in composites averaged over week 3 following each phase of the MJO are  
335 shown. Each row corresponds to a phase of the MJO. (**Left column** and **Right-middle column**)  
336 show easterly QBO composites minus westerly QBO composites. The displayed latitudinal range  
337 is from the equator to 90°N. (**Left-middle column and Right column**) show La Niña composites  
338 minus the El Niño composites. The displayed latitudinal range is from 30°S to 60°N. The  
339 displayed longitudinal range for all columns is from 90°E to 270°E. Only days during November-  
340 February are composited. (**Left column** and **Left-middle column**) Black vectors depict  
341 anomalous IVT<sub>AR</sub> ( $\text{kg m}^{-1} \text{ s}^{-1}$ ), with only those vectors with magnitudes  $\geq 10 \text{ kg m}^{-1} \text{ s}^{-1}$  and with  
342 either component statistically significant at the 2% level plotted. A reference vector is located in  
343 the upper right corner of the (**top-left panel**). Two iterations of nine-point local smoothing were  
344 applied to the components of the vectors before plotting. Shading depicts 500-hPa geopotential  
345 height anomalies, with its statistical significance at the 2% level indicated by stippling, as  
346 determined by a Monte Carlo simulation (Text S11). (**Right-middle column** and **Right column**)  
347 Shading depicts OLR anomalies, with its statistical significance at the 2% level indicated by  
348 stippling, as determined by a Monte Carlo simulation (Text S11). Sample sizes are provided in  
349 Tables S1 and S6. The figure derives from ERA-Interim data [*Dee et al.*, 2011].

OMI MJO Phase	QBO Independent		Easterly QBO		Westerly QBO	
	n	n <sub>eq</sub>	n	n <sub>eq</sub>	n	n <sub>eq</sub>
1	291	52	104	19	113	22
2	333	59	125	20	119	23
3	364	64	124	22	175	28
4	358	68	123	23	147	29
5	278	59	111	20	95	22
6	337	63	115	20	134	28
7	348	65	109	20	162	31
8	317	60	130	20	135	28

350

351   **Table S1.** Samples sizes  $n$  and equivalent sample sizes  $n_{eq}$  are shown for the days composited in  
 352   Figures 2, 3, S2, S4, S6, and S7. Because the MJO may reside in a certain phase several  
 353   consecutive days in a row, our samples of size  $n$  days often have a certain degree of  
 354   autocorrelation imbedded in them. To correct for this when calculating statistical significance, we  
 355   count the number of unique groupings of consecutive days within the sample to determine  $n_{eq}$ .

OMI MJO Phase	Easterly QBO	Westerly QBO
	n	n
7,8	89	80
6,7	85	81
5,6	103	89
4,5	98	102
3,4	84	80
2,3	94	59
1,2	91	77
8,1	90	84

356

357   **Table S2.** Samples sizes  $n$  for the number of reforecasts included in the calculation of the LSS in  
 358   Figures 4 and S3.

RMM MJO Phase	QBO		Easterly QBO		Westerly QBO	
	n	n <sub>eq</sub>	n	n <sub>eq</sub>	n	n <sub>eq</sub>
1	233	65	91	23	79	27
2	300	81	96	26	117	32
3	421	92	138	31	181	39
4	347	100	109	31	164	47
5	332	97	132	29	150	51
6	403	106	133	32	197	55
7	442	104	140	32	196	48
8	299	79	120	31	100	30

359

360 **Table S3.** As in Table S1 but for Figure S5.

361

i	c <sub>i</sub>	n <sub>i</sub>	p <sub>i</sub>	q <sub>i</sub>	LS	L <sub>S</sub> <sub>ref</sub>	LSS
0	0	0	0.010417	0.391555			
1	1	0	0.010417	0.271018			
2	2	1	0.093750	0.160856			
3	3	5	0.427083	0.112336	-0.85	-2.19	1.34
4	4	4	0.343750	0.044286			
5	5	1	0.093750	0.016822			
6	6	0	0.010417	0.003090			
7	7	0	0.010417	0.000038			

362

363 **Table S4.** Tabulation of the values used to calculate the LSS for the prediction of AR strikes per  
 364 week on Alaska by a single ECMWF reforecast ensemble system [Vitart *et al.*, 2017] run that  
 365 initialized at 0000 UTC 3 December 2009 is shown. The values correspond to the first week of  
 366 the model run (4 to 10 December 2009). Definitions of the values are provided in Text S8. The  
 367 highlighted row indicates the LSS that results from the observed outcome of 3 AR strikes.

368

	Neutral ENSO	La Niña	El Niño
Neutral QBO	11	6	14
Easterly QBO	25	12	9
Westerly QBO	27	18	26

369   **Table S5.** Counts of November-February months from 1979-2015 according to their QBO and  
370   ENSO states. The table derives from ERA-Interim data [Dee *et al.*, 2011] and the Niño3.4 index  
371   obtained from the National Centers for Environmental Prediction/Climate Prediction Center.

OMI MJO Phase	ENSO Independent		La Niña		El Niño	
	n	n <sub>eq</sub>	n	n <sub>eq</sub>	n	n <sub>eq</sub>
1	291	52	81	14	89	16
2	333	59	90	16	106	20
3	364	64	89	16	134	21
4	358	68	104	18	132	25
5	278	59	71	14	89	22
6	337	63	76	14	122	22
7	348	65	98	15	112	21
8	317	60	85	14	96	18

372

373   **Table S6.** As in Table S1 but for Figure S7.